




Theoretical analysis of a multi-grating-based cross-dispersed spatial heterodyne spectrometer

QIHANG CHU,^{1,2,3}  XIAOTIAN LI,^{1,2,3,*} YUQI SUN,^{1,2,3}
JIRIGALANTU,^{1,2,3} CI SUN,^{1,2,3} JUN CHEN,^{1,2,3}  FUGUAN LI,^{1,2,3}
AND BAYANHESHIG^{1,2,3}

¹Changchun Institute of Optics, Fine Mechanics and Physics, Chinese Academy of Sciences, Changchun, Jilin 130033, China

²University of Chinese Academy of Sciences, Beijing 100049, China

³National Engineering Research Center for Diffraction Gratings Manufacturing and Application, Changchun, Jilin 130033, China

*lixiaotian@ciomp.ac.cn

Abstract: This paper presents a multi-grating-based cross-dispersed spatial heterodyne spectrometer (MGCDSHS). The principle of generation of two-dimensional interferograms for two cases, where the light beam is diffracted by one sub-grating or two sub-gratings, is given and equations for the interferogram parameters in these two cases are derived. An instrument design with numerical simulations is presented that demonstrates the spectrometer's ability to simultaneously record separate interferograms corresponding to different spectral features with high resolution over a broad spectral range. The design solves the mutual interference problem caused by overlapping of the interferograms, and also provides the high spectral resolution and broad spectral measurement range that cannot be achieved using conventional SHSs. Additionally, by introducing cylindrical lens groups, the MGCDSHS solves the throughput loss and light intensity reduction problems caused by direct use of multi-gratings. The MGCDSHS is compact, highly stable, and high-throughput. These advantages make the MGCDSHS suitable for high-sensitivity, high-resolution, and broadband spectral measurements.

© 2023 Optica Publishing Group under the terms of the [Optica Open Access Publishing Agreement](#)

1. Introduction

As a new type of static spatial modulation spectrometer, the spatial heterodyne spectrometer (SHS) integrates the characteristics of a diffraction grating with those of a Fourier transform interferometer [1–3]. The SHS can heterodyne interference fringes with a frequency corresponding to the Littrow angle of the diffraction grating [2]. This spectrometer is used widely in the measurement of quantities that include chemical compounds [4–6], minerals [7–9], and emissions from astrophysical targets [10–12]. The Nyquist sampling theorem indicates that there is an inverse relationship between the requirements for the spectral range and the spectral resolution in the SHS [13]. Additionally, as a Fourier transform-type interferometer, the SHS is able to measure interferograms generated by multiplexing of the interference fringes of all spectral features [14,15]. The two characteristics described above cause two problems in practical applications of the SHS.

First, the mutual restraint between the spectral range and the spectral resolution limits further improvements in the spectral performance. The tunable SHS is able to record high resolution and broadband spectral information by performing multiple measurements of different spectral ranges through use of moving parts [16–18], but this leads to insufficient instrument stability and thus it cannot obtain all the spectral information required in a single measurement. Replacement of the conventional gratings in the spectrometer with multi-gratings consisting of multiple sub-gratings

with different groove densities in the SHS can break through the above limitation and allow broadband, high-resolution spectra to be acquired in a single-shot measurement [19–21]. On each sub-grating, only light with a spectral feature that lies within the spectral range of the sub-grating can be diffracted to generate useful interference fringes and transformed into a corresponding spectrum; the remaining light cannot form useful interference fringes. Because the polychromatic incident light beam irradiates the multi-gratings directly, the intensity of the light that does not irradiate the corresponding sub-grating is wasted. This waste results in a loss of throughput and ultimately in a reduction in the intensity of the interference fringes, which will then be exacerbated when there are additional sub-gratings contained in a multi-grating.

The second problem is that, as a result of the overlapping of the interferograms caused by the multiplexing characteristic of the SHS, the signal-to-noise ratio will decrease as the number of spectral features in the spectrum increases [22,23]. The most serious problem caused by the overlapping problem is that all spectral features in the measurement range cannot be measured if there is a spectral feature with oversaturated high-intensity light. To overcome this overlapping problem, Sheinis et al. used the combination of a cross-dispersing prism with echelle gratings of high orders [24] to separate the interferograms from 17 different wavebands, while Egan et al. paired an Amici prism spectrometer in series with an SHS [25] to achieve cross-dispersion. However, the dispersion ability of the prism is not as good as that of a grating. A long optical path or multiple refractions would be required to achieve a good dispersion effect when using a prism, which would then lead to an instrument with excessive volume or weakening of the intensity of the incident light. To achieve a better cross-dispersion effect, we previously proposed the cross-dispersed SHS (CDSHS) with one-dimensional interferograms [26]. The CDSHS can use different rows on the detector to record interferograms with different spectral features by introducing a longitudinal diffraction grating. Although the CDSHS offers advantages in terms of cross-dispersion, there is still considerable room for improvement in the broadband high-resolution measurements mentioned above. In addition, the model of the SHS used in the CDSHS was based on the basic grating equation and can only measure a one-sided waveband of the Littrow wavelength because of the ambiguity related to wavelengths that are symmetrical to the Littrow wavelength [2]; this means that this model is not suitable for measurements performed using multi-gratings.

In this paper, a multi-grating-based CDSHS (MGCDHS) is described. The principle and the mathematical model of the MGCDHS are derived and a numerical simulation treatment with a theoretical design is presented. The spectrometer design replaces the conventional grating used in the SHS with the multi-grating to realize both a broad spectral range and high spectral resolution simultaneously. The combination of the cylindrical lens group with the reflection grating can reduce the size of the light beam in the longitudinal plane and distribute light beams with different spectral features to corresponding sub-gratings with corresponding spectral ranges, and this allows both the loss of throughput and the intensity reduction of the fringes to be avoided. The designed spectrometer can distribute the two-dimensional interferograms corresponding to different spectral features recorded by different position on a detector with no interference, which overcomes the disadvantage of the overlapping problem and ensures that other spectral features can still be measured under the condition of the oversaturated high-intensity light at a specific spectral feature. Rolling one multi-grating around its central normal expands the effective spectral range for each sub-grating and makes the model suitable for the multi-grating, and introduction of the conical diffraction equation can enable a more accurate mathematical model of the two-dimensional interferogram generated by the MGCDHS to be built. A numerical simulation over a wavelength range from 530 nm to 645 nm is presented. The component design process and the data used in the simulation process are given in detail, and the simulation results are presented in the form of a beam distribution schematic, the interferograms on the detector,

and the corresponding detailed spectrum. Finally, conclusions drawn from the work in this article are given.

2. Principle

2.1. Light beam diffracted by one sub-grating

Figure 1(a) illustrates the optical layout of the MGCDSHS, which integrates a cylindrical lens group with a reflection grating, a multi-grating-based SHS (MGSHS), and a single cylindrical lens. The MGSHS integrates one beam splitter with two multi-gratings, designated MG_1 and MG_2 , which combine multiple independent sub-gratings with different groove densities, as shown in Fig. 1(b), and are set in the Littrow condition. Multi-grating MG_1 is rolled by a small angle around the center normal of its groove facet to generate two-dimensional fringes. Figure 2(a) and 2(b) illustrate the equivalent light paths for a polychromatic light beam traveling to and leaving from multi-grating MG_i ($i = 1, 2$) in the longitudinal plane and in the lateral plane, respectively. The collimated incident light beam from the sample is first reduced in size by the cylindrical lens group and then dispersed into several light beams by reflection grating G_r in the longitudinal plane (i.e., in the x - y plane). Each light beam corresponds to a different spectral feature and each beam is divided into two light beams by the beam splitter. These two groups of light beams then travel to and are diffracted by the corresponding gratings in multi-gratings MG_1 and MG_2 of the MGSHS in the lateral plane (i.e., in the z - x plane). After they leave the multi-gratings and are combined by the beam splitter, these coherent beams are collimated by the cylindrical lens set after the MGSHS. Finally, the two-dimensional fringes corresponding to the different spectral features produced by the interference of these coherent beams are received independently by different regions on the area-array detector. The detection plane is set at a distance away from the back focal length of the cylindrical lens.

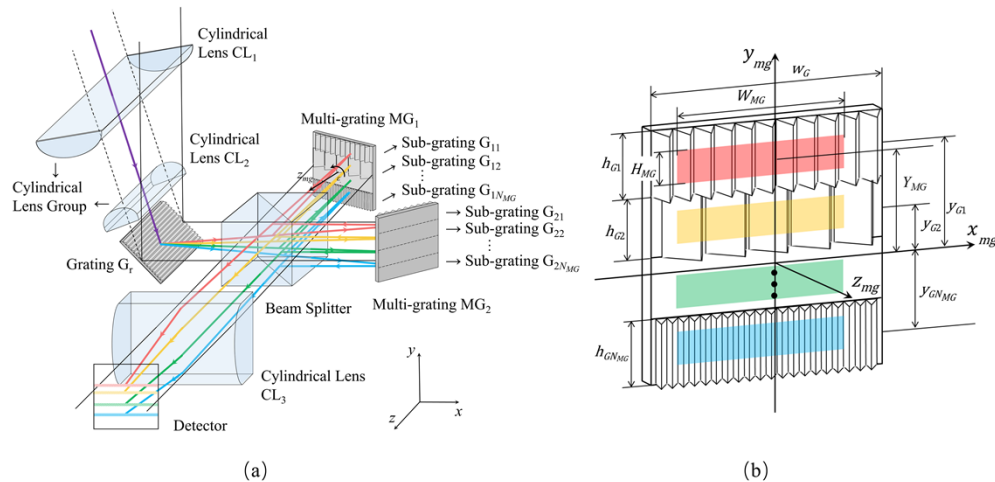


Fig. 1. (a) Optical layout of the multi-grating-based cross-dispersed spatial heterodyne spectrometer (MGCDSHS), and (b) the diagram of the light beams on the coordinate system of the multi-grating.

Throughout this paper, we assume that each row of the area-array detector is oriented parallel to the x -axis of the detector plane, and that each column of the area-array detector is oriented parallel to the y -axis of the detector plane. Let the polychromatic light source cover the wavenumber range from σ_{\min} to σ_{\max} (i.e., the wavelength range from $\lambda_{\min} = 1/\sigma_{\max}$ to $\lambda_{\max} = 1/\sigma_{\min}$).

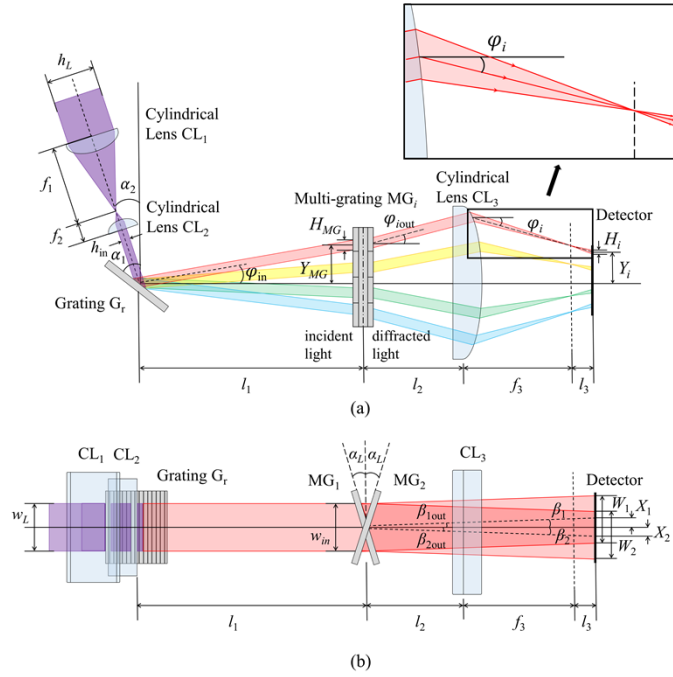


Fig. 2. Equivalent light path diagrams before and after multi-grating MG_i ($i = 1, 2$) for the different wavenumbers (a) in the longitudinal plane and (b) in the lateral plane.

Figure 1(b) shows the diagram of the multi-grating, which is the most important component in the MGSLS. For a multi-grating that combines N_{MG} gratings with different groove densities, each sub-grating contains a unique Littrow wavenumber σ_{jL} and associated groove density $1/d_j$ ($j = 1, 2, \dots, N_{MG}$). The Littrow condition for each sub-grating in the multi-gratings satisfies the following:

$$2\sigma_{jL} \sin \alpha_L = \frac{1}{d_j} \quad j = 1, 2, \dots, N_{MG} \quad (1)$$

where α_L is the Littrow angle of the multi-grating. From Eq. (1), when the Littrow angle is determined, the relationship between the Littrow wavenumber and the groove density for each sub-grating can be written as follows:

$$1/d_1 : 1/d_2 : \dots : 1/d_{j-1} : 1/d_j = \sigma_1 : \sigma_2 : \dots : \sigma_{j-1} : \sigma_j \quad (2)$$

Let w_{Gj} and h_{Gj} denote the width and height of each sub-grating, and let w_{MG} and h_{MG} denote the width and height of the multi-grating, respectively. By assuming that all the sub-gratings have the same width, the different regions of the multi-gratings can be expressed as:

$$MG(x_{mg}, y_{mg}) = \sum_{j=1}^{N_{MG}} \text{rect} \left(\frac{x_{mg}}{w_{Gj}} \right) \text{rect} \left(\frac{y_{mg} - y_{Gj}}{h_{Gj}} \right) = \text{rect} \left(\frac{x_{mg}}{w_{MG}} \right) \text{rect} \left(\frac{y_{mg} - y_{G1} + y_{GN_{MG}} - \frac{h_{G1} - h_{GN_{MG}}}{2}}{y_{G1} - y_{GN_{MG}} + \frac{h_{G1} + h_{GN_{MG}}}{2}} \right) = \text{rect} \left(\frac{x_{mg}}{w_{MG}} \right) \text{rect} \left(\frac{y_{mg} - y_{MG}}{h_{MG}} \right) \quad (3)$$

where y_{Gj} is the y_{mg} -axis position of the center of each sub-grating G_{ij} , the x_{mg} -axis position of the center of each sub-grating is on the y_{mg} -axis, and y_{MG} is the y_{mg} -axis position of the center of the multi-grating. The relationship between h_{Gj} , h_{Gj-1} and y_{Gj-1} , y_{Gj} for each pair of adjacent

gratings G_{ij-1} and G_{ij} can be expressed as:

$$y_{G_{j-1}} - y_{G_j} = \frac{h_{G_{j-1}}}{2} + \frac{h_{G_j}}{2} \quad j = 2, \dots, N_{MG} \quad (4)$$

In Fig. 2, a typical incident light beam with height h_L and width w_L is drawn, and the light is first converged by cylindrical lens CL_1 with focal length f_1 and then collimated by cylindrical lens CL_2 with focal length f_2 (where $f_1 > f_2 > 0$) in the longitudinal plane, and the two cylindrical lenses are placed according to the sum of their back focal lengths. Therefore, after traveling through the cylindrical lens group, the height h_{in} and the width w_{in} of the light beam can be expressed as:

$$\begin{cases} h_{in} = \frac{f_2}{f_1} h_L \\ w_{in} = w_L \end{cases} \quad (5)$$

This incident light beam is then dispersed into several beams in the longitudinal direction with different wavenumbers by reflection grating G_r . The equation for the dispersion is given by:

$$\sin(\alpha_1 - \varphi_{in}) - \sin\left(\frac{\pi}{2} - \alpha_1 + \alpha_2\right) = \frac{1}{\sigma d_r} \quad (6)$$

where $1/d_r$ is the groove density of grating G_r , σ is the wavenumber of the incident light, and α_1 and α_2 are the tilt angle of grating G_r and the deflection angle of the incident light beam, respectively. When the light beams pass into the MGSHS, the angle of incidence in the longitudinal plane φ_{in} can be obtained using:

$$\varphi_{in}(\sigma) = \alpha_1 - \sin^{-1}\left(\frac{1}{\sigma d_r} + \cos(\alpha_1 - \alpha_2)\right) \quad (7)$$

According to Eq. (7), when the polychromatic light enters the MGSHS, the y_{mg} -axis position of the incident beam and the sizes of the beams on the multi-grating MG_i ($i = 1, 2$) vary with the wavenumber, as shown in Fig. 2, and these parameters can be expressed as:

$$Y_{MG}(\sigma) = l_1 \tan \varphi_{in} \quad (8)$$

$$\begin{cases} H_{MG}(\sigma) = h_{in} \frac{\cos(\alpha_1 - \varphi_{in})}{\sin(\alpha_1 - \alpha_2) \cos \varphi_{in}} \\ W_{MG} = \frac{w_{in}}{\cos \alpha_L} \end{cases} \quad (9)$$

where Y_{MG} is the y_{mg} -axis position of the center of the light beams on multi-grating MG_i , and H_{MG} and W_{MG} are the height and width, respectively, of the light beams on the multi-grating MG_i . It is assumed that the widths and heights of the light beams and the multi-gratings satisfy the following:

$$\begin{cases} w_G > W_{MG} \\ h_{G_j} > H_{MG} \end{cases} \quad (10)$$

For the first situation shown in Fig. 3, the light beam is diffracted by only one sub-grating, designated G_{ij} , on the multi-grating MG_i , and by combining Eq. (8) with Eq. (9), the function of the diffracted light beam on the grating can be expressed as:

$$L_{S1}(x_m, y_m, \sigma) = \text{rect}\left(\frac{x_m}{W_{S1}}\right) \text{rect}\left(\frac{y_m - Y_{S1}}{H_{S1}}\right) = \text{rect}\left(\frac{x_m}{W_{MG}}\right) \text{rect}\left(\frac{y_m - Y_{MG}}{H_{MG}}\right) \quad (11)$$

where Y_{S1} is the y_{mg} -axis position of the center of the light beam on grating G_{ij} , and H_{S1} and W_{S1} are the height and width of this light beam, respectively.

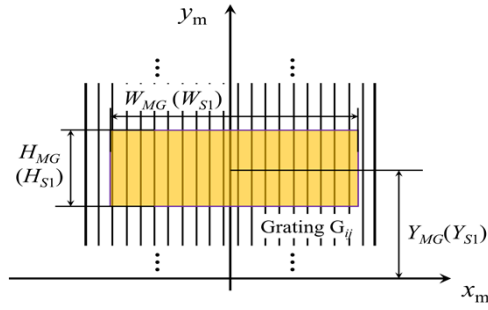


Fig. 3. Schematic diagram of light beam diffracted by one sub-grating G_{ij} .

Figure 4 illustrates the wavevector components in the Cartesian coordinate system and the incoming and outgoing wavevectors for each sub-grating. The multi-gratings are positioned such that the z_{mg} -axis intersects them at the center normal of the groove facet. As shown in Fig. 4(a), x_c , y_c , and z_c represent the three coordinate axes of Cartesian coordinate system, the optical axis lies in x_c - z_c plane and has an angle of α with the z_c -axis, and the wavevector can be decomposed into:

$$\begin{cases} k_x = 2\pi\sigma \cos \varphi \sin(\beta + \alpha) = 2\pi\sigma \sin \theta \cos \rho \\ k_y = 2\pi\sigma \sin \varphi = 2\pi\sigma \sin \theta \sin \rho \\ k_z = 2\pi\sigma \cos \varphi \cos(\beta + \alpha) = 2\pi\sigma \cos \theta \end{cases} \quad (12)$$

where β is the angle between the projection of the wavevector on the x_c - z_c plane and the optical axis, φ is the angle between the wavevector and the x_c - z_c plane, ρ is the azimuth angle between the projection of the wavevector on the x_c - y_c plane and the x_c -axis, and θ is the polar angle between the wavevector and the z_c -axis.

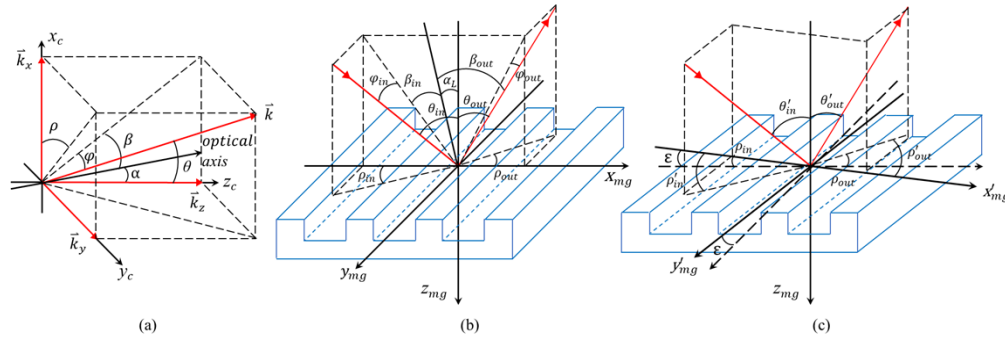


Fig. 4. (a) Wavevector components in Cartesian coordinate system, and diagrams of the incoming and outgoing wavevectors of a multi-grating (b) with no roll and (c) with a roll angle ϵ in the x - y plane.

Because of the diffraction of the reflection grating G_r , the propagation direction of the incident light beams no longer lies perpendicular to the facet of the grating groove, and the incoming and outgoing wavevectors are distributed over a conical plane [27–29]. Based on Eq. (12), the generalized grating equations based on conical diffraction for the multi-gratings can be expressed

as:

$$\begin{cases} \sin \theta_{out} \cos \rho_{out} + \sin \theta_{in} \cos \rho_{in} = \frac{1}{\sigma d_j} \\ \sin \theta_{out} \sin \rho_{out} + \sin \theta_{in} \sin \rho_{in} = 0 \end{cases} \quad (13)$$

where ρ_{in} and ρ_{out} are the angle of incidence and the diffraction azimuth angle, respectively; and θ_{in} and θ_{out} are the angle of incidence and the diffraction polar angle, respectively. Substituting $\alpha = \alpha_L$, and the incidence angles $\beta_{in} = 0$ and $\varphi_{in}(\sigma)$ in Eq. (12), combining with Eq. (13) can calculate the diffraction angles $\beta_{1out}(\sigma)$, $\beta_{2out}(\sigma)$, $\varphi_{1out}(\sigma)$, and $\varphi_{2out}(\sigma)$.

As shown in Fig. 2(a), after they return from their corresponding multi-gratings and leave the beam splitter, the light beams are then converged by cylindrical lens CL₃, and are finally received by the detector. According to the geometrical relationship and the characteristics of the cylindrical lens, the refraction angles after the cylindrical lens in the longitudinal plane can be expressed as:

$$\begin{cases} \tan \varphi_1 = \frac{Y_{S1} + (f_3 - l_2) \tan \varphi_{1out}}{f_3} \\ \tan \varphi_2 = \frac{Y_{S1} + (f_3 - l_2) \tan \varphi_{2out}}{f_3} \end{cases} \quad (14)$$

where φ_1 and φ_2 are the refraction angles in the longitudinal plane of the central rays of the converged light beams that are diffracted by multi-gratings MG₁ and MG₂, respectively; l_1 is the distance between reflection grating G_r and multi-grating MG₁ or MG₂, l_2 is the distance between the multi-grating and cylindrical lens CL₃, and f_3 is the back focal length of cylindrical lens CL₃.

When the coherent light beams are received by the detector as shown in Fig. 5, the y-axis positions of the central rays of the light beams and the heights of the light beams at the detector plane can be written as follows:

$$\begin{cases} Y_1(\sigma) = Y_{S1} - l_2 \tan \varphi_{1out} - (f_3 + l_3) \tan \varphi_1 \\ Y_2(\sigma) = Y_{S1} - l_2 \tan \varphi_{2out} - (f_3 + l_3) \tan \varphi_2 \end{cases} \quad (15)$$

$$\begin{cases} H_1(\sigma) = \frac{l_3}{f_3} H_{S1} \cos \varphi_{1out} \\ H_2(\sigma) = \frac{l_3}{f_3} H_{S1} \cos \varphi_{2out} \end{cases} \quad (16)$$

where Y_1 and Y_2 are the y-axis positions of the centers of these light beams at the detector plane, H_1 and H_2 are the heights of the light beams at the detector plane, and l_3 is the distance between the back focal plane of cylindrical lens CL₃ and the detector.

As shown in Fig. 2(b), in the lateral plane, the diffracted light beams are not affected by the cylindrical lens, and they travel to the detector with angles $\beta_1 = \beta_{1out}$ and $\beta_2 = \beta_{2out}$. At the detector plane, the x-axis positions of the central rays of the light beams and the widths of the light beams can be expressed as follows:

$$\begin{cases} X_1(\sigma) = (l_2 + f_3 + l_3) \tan \beta_1 \\ X_2(\sigma) = (l_2 + f_3 + l_3) \tan \beta_2 \end{cases} \quad (17)$$

$$\begin{cases} W_1(\sigma) = W_{S1} \cos(\alpha_L - \beta_1) \\ W_2(\sigma) = W_{S1} \cos(\alpha_L - \beta_2) \end{cases} \quad (18)$$

where X_1 and X_2 are the x-axis positions of the centers of the light beams at the detector plane, and W_1 and W_2 are the widths of the light beams at the detector plane.

As Fig. 5 shows, as a result of the conical diffraction, the two groups of light beams partially interfere at the detector plane. Combining Eqs. (15)–(18) can calculate the width W_I and the

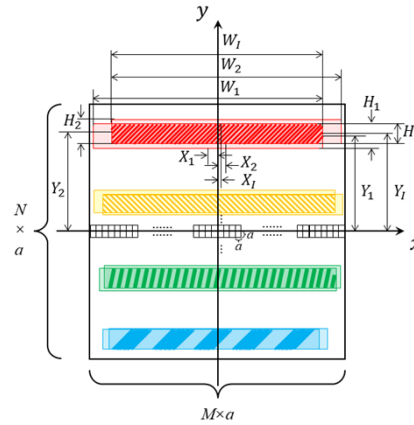


Fig. 5. Diagrams of the two-dimensional interferograms corresponding to the different spectral features on the area-array detector.

height H_I of the interferograms, and the positions of the interferograms at the x -axis X_I and the y -axis Y_I , respectively. To obtain sufficient data from the interferograms while preventing the interferograms that correspond to different spectral features from overlapping each other, it is necessary to make a trade-off in terms of the sizes of the interferograms. As the schematic diagram in Fig. 5 shows, at the detector, the size of each pixel is a , and the numbers of pixels in each row and each column are M and N , respectively. Therefore, the width and the height of the detector can be denoted by $M \times a$ and $N \times a$, respectively. Assuming that the minimum width of the interferograms is m ($m \leq 1$) times the width of the detector, and that the minimum height of the interferograms is n ($n > 1$) times the pixel size, the relationship between the parameters of each interferogram and the parameters of the detector can be limited by the following:

$$|Y_I(\sigma_{\max}) - Y_I(\sigma_{\min})| + \frac{1}{2}(H_I(\sigma_{\max}) + H_I(\sigma_{\min})) \leq Na \quad (19)$$

$$H_I(\sigma) \geq na \quad (20)$$

$$W_I(\sigma) \geq mMa \quad (21)$$

The areas of the interferograms corresponding to the different spectral features on the detector can be calculated using:

$$L_I(x, y, \sigma) = \text{rect}\left(\frac{x - X_I}{W_I}\right) \text{rect}\left(\frac{y - Y_I}{H_I}\right) \quad (22)$$

The intensity distribution produced by the interference of two coherent light beams with the same intensity that are characterized by the wavevectors \vec{k}_1 and \vec{k}_2 is:

$$I = B_0(1 + \cos((\vec{k}_1 - \vec{k}_2) \cdot \vec{r})) = B_0(1 + \cos((k_{1x} - k_{2x}) \cdot x + (k_{1y} - k_{2y}) \cdot y + (k_{1z} - k_{2z}) \cdot z)) \quad (23)$$

where $B_0/2$ is the intensity of each light beam and \vec{r} is the displacement vector. By referring to the wavevector decomposition diagram shown in Fig. 4(a), the angle between the optical axis and the z -axis $\alpha=0$, substituting Eq. (12) into Eq. (23), and combining the resulting equation with Eq. (22), we can obtain the final intensity distribution on the detector plane (i.e., x - y plane) for a

polychromatic source of MGCDSSHs as follows:

$$I(x, y) = \int_0^{\infty} B(\sigma) \cdot (1 + \cos(2\pi\sigma((\cos \varphi_1 \sin \beta_1 - \cos \varphi_2 \sin \beta_2)x + (\sin \varphi_1 - \sin \varphi_2)y))) \text{rect}\left(\frac{x-X_I}{W_I}\right) \text{rect}\left(\frac{y-Y_I}{H_I}\right) d\sigma \quad (24)$$

Having been summarized previously by other researchers in the literature, the spectral resolution δ_σ and the spectral range Δ_σ of a conventional SHS with two-dimensional interference fringes are given by:

$$\delta_\sigma = \frac{1}{4W_E \sin \alpha_L} \quad (25)$$

$$\Delta_\sigma = M\delta_\sigma = \frac{M}{4W_E \sin \alpha_L} = \sigma_{\max} - \sigma_{\min} \quad (26)$$

where W_E is the effective light beam width on the grating, which can be calculated using:

$$W_E = w_{in}/\cos\alpha_L = w_L/\cos\alpha_L. \quad (27)$$

As Eq. (26) shows, the inverse relationship between the spectral range and the spectral resolution cannot be broken by using only a conventional grating in an SHS. By replacing the conventional gratings with multi-gratings consisting of N_{MG} (where $N_{MG} \geq 2$) gratings with different groove densities and assuming that the effective spectral range of each grating is equal and that these ranges are just not covered by each other, the overall spectral range Δ_{MG} can then be rewritten as [20]:

$$\Delta_{MG} = \Delta_1 + \Delta_2 + \dots + \Delta_{N_{MG}} = N_{MG}M\delta_\sigma \quad (28)$$

where $\Delta_j = \sigma_{j\max} - \sigma_{j\min}$ ($j = 1, 2, \dots, N_{MG}$) is the spectral range of each sub-grating G_{ij} in the multi-gratings MG_i ($i = 1, 2$). In this situation, the effective wavenumber range for each grating G_{ij} is from $\sigma_{j\min}$ to $\sigma_{j\max}$, and $\sigma_{j-1\min} = \sigma_{j\max}$.

2.2. Light beam diffracted by two sub-gratings

Figure 3 shows a general case where the beams are diffracted by a single sub-grating of the multi-grating in the MGCDSSHs. However, because of the mosaic structure of the gratings, few light beams travel to the boundary of the mosaic after being dispersed by the reflection grating G_r . For the advanced case shown in Fig. 6(a), the light beam is diffracted by two different gratings, designated G_{ij-1} and G_{ij} , with different groove densities on the multi-grating MG_i . In this case, the light beam can no longer be regarded as a single beam after diffraction, and the function for the diffracted light beams on the grating can be expressed as:

$$L_{S2}(x_{mg}, y_{mg}, \sigma) = \begin{cases} L_{S21}(x_{mg}, y_{mg}, \sigma) = \text{rect}\left(\frac{x_{mg}}{W_{S21}}\right) \text{rect}\left(\frac{y_{mg}-Y_{S21}}{H_{S21}}\right) = \text{rect}\left(\frac{x_{mg}}{W_{MG}}\right) \text{rect}\left(\frac{Y_{MG}+Y_{Gj-1} + \frac{H_{MG}-h_{Gj-1}}{4}}{2}\right) & \text{on grating } G_{ij-1} \\ L_{S22}(x_{mg}, y_{mg}, \sigma) = \text{rect}\left(\frac{x_{mg}}{W_{S22}}\right) \text{rect}\left(\frac{y_{mg}-Y_{S22}}{H_{S22}}\right) = \text{rect}\left(\frac{x_{mg}}{W_{MG}}\right) \text{rect}\left(\frac{Y_{MG}-Y_{Gj-1} + \frac{H_{MG}+h_{Gj-1}}{2}}{2}\right) & \text{on grating } G_{ij} \end{cases} \quad (29)$$

where Y_{S21} and Y_{S22} are the y_{mg} -axis positions of the centers of the light beams on gratings G_{ij-1} and G_{ij} , respectively. H_{S21} and W_{S21} are the height and the width of this light beam on grating G_{ij-1} , and H_{S22} and W_{S22} are the height and the width of this light beam on grating G_{ij} , respectively.

For the first part of the light beam diffracted by grating G_{ij-1} with $1/d_{j-1}$, after the diffraction angles are first calculated using Eq. (12) and Eq. (13), and the substitutions of Y_{S1} , H_{S1} , and W_{S1} with Y_{S21} , H_{S21} , and W_{S21} , respectively, are made in Eqs. (14)-(18) to determine the angles $\varphi_{i1} = \varphi_i$ and $\beta_{i1} = \beta_i$ ($i = 1, 2$), the positions $X_{I1} = X_I$ and $Y_{I1} = Y_I$, and the parameters $H_{I1} = H_I$ and $W_{I1} = W_I$ for the corresponding interferogram. The interferogram corresponding to the second part of the light beam diffracted by grating G_{ij} with $1/d_j$ can also be determined using the above analysis

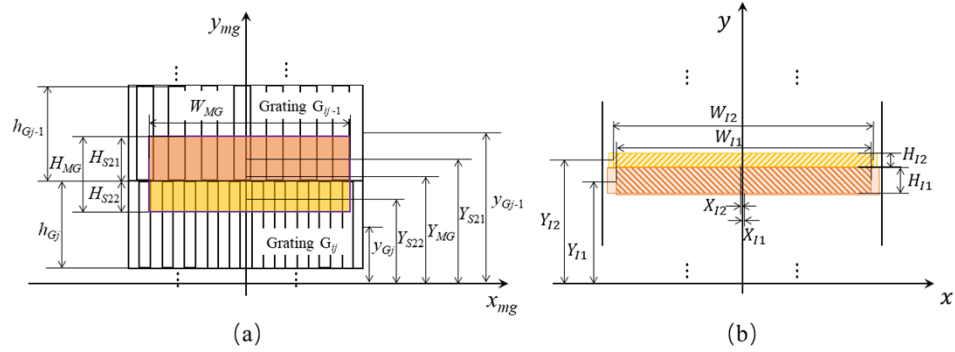


Fig. 6. Schematic diagram of (a) light beam diffracted by two gratings, G_{ij-1} and G_{ij} , and (b) corresponding two-dimensional interferograms on the detector.

by calculating the diffraction angles using Eq. (12) and Eq. (13) with groove density $1/d_j$, and then making the substitutions of Y_{S1} , H_{S1} , and W_{S1} with Y_{S22} , H_{S22} , and W_{S22} , respectively, to finally determine $\varphi_{i2}=\varphi_i$, $\beta_{i2}=\beta_i$, $X_{I2}=X_I$, $Y_{I2}=Y_I$, $H_{I2}=H_I$, and $W_{I2}=W_I$. These two parts of the interferograms finally form a mosaic interferogram with this wavenumber on the detector, which can be calculated using:

$$L_I(x, y, \sigma) = \text{rect}\left(\frac{x - X_{I1}}{W_{I1}}\right) \text{rect}\left(\frac{y - Y_{I1}}{H_{I1}}\right) + \text{rect}\left(\frac{x - X_{I2}}{W_{I2}}\right) \text{rect}\left(\frac{y - Y_{I2}}{H_{I2}}\right) \quad (30)$$

As shown in Fig. 6(b), and according to Eqs. (20) and (21), the trade-off between the parameters of the mosaic interferogram in this advanced case can be limited by the following:

$$H_{I1}(\sigma) + H_{I2}(\sigma) \geq na \quad (31)$$

$$\begin{cases} W_{I1}(\sigma) \geq mMa \\ W_{I2}(\sigma) \geq mMa \end{cases} \quad (32)$$

Based on Eq. (24), we can determine the final intensity distribution on the detector plane in the advanced case to be:

$$I(x, y) = \int_0^\infty B(\sigma) \cdot \left((1 + \cos(2\pi\sigma((\cos\varphi_{11} \sin\beta_{11} - \cos\varphi_{21} \sin\beta_{21})x + (\sin\varphi_{11} - \sin\varphi_{21})y))) \text{rect}\left(\frac{x-X_{I1}}{W_{I1}}\right) \text{rect}\left(\frac{y-Y_{I1}}{H_{I1}}\right) \right. \\ \left. + (1 + \cos(2\pi\sigma((\cos\varphi_{12} \sin\beta_{12} - \cos\varphi_{22} \sin\beta_{22})x + (\sin\varphi_{12} - \sin\varphi_{22})y))) \text{rect}\left(\frac{x-X_{I2}}{W_{I2}}\right) \text{rect}\left(\frac{y-Y_{I2}}{H_{I2}}\right) \right) d\sigma \quad (33)$$

When the incident light beam of the MGSMS with height h_{in} and width w_{in} is dispersed by the reflection grating G_r in the longitudinal direction and travels to the multi-gratings, the beams are distributed from top to bottom on the multi-gratings according to their wavenumbers. The beams with larger wavenumbers are distributed in the upper part, and the beams with smaller wavenumbers are distributed in the lower part, and this is the same for the multi-grating and for each sub-grating. As shown in Fig. 6(a), a light beam being diffracted by two different gratings G_{ij-1} and G_{ij} will cause losses of both throughput and intensity when the effective spectral ranges of each grating are just not overlapped. Therefore, it is necessary to set sufficient effective spectral ranges for the sub-gratings and cause them to be partially covered (i.e., $\sigma_{j-1 \min} < \sigma_{j \max}$) if we are to obtain the correct spectra from the intensity distributions of the two parts of the interferogram in this case.

To ensure that all spectral features can be detected and that the losses in the throughput and the intensity can be avoided, the light beam on the boundary between two gratings should be

measured by the two gratings simultaneously (i.e., the wavenumber corresponding to the beam is within the spectral range that is covered); then, the relationship between the parameters of each pair of adjacent sub-gratings and the wavenumbers of the light beams being diffracted by these two gratings can be limited by the following:

$$\begin{cases} Y_{MG}(\sigma_{j\max}) - \frac{H_{MG}(\sigma_{j\max})}{2} \geq y_{Gj} + \frac{h_{Gj}}{2} \quad j = 2, \dots, N_{MG} \\ Y_{MG}(\sigma_{j\min}) + \frac{H_{MG}(\sigma_{j\min})}{2} \leq y_{Gj} - \frac{h_{Gj}}{2} \quad j = 1, 2, \dots, N_{MG} - 1 \end{cases} \quad (34)$$

3. Numerical simulation with an example

If it is assumed that the wavelength range for the polychromatic incident light is from 530 nm to 645 nm, i.e., that its wavenumber range is from $15503.8760 \text{ cm}^{-1}$ to $18867.9245 \text{ cm}^{-1}$, then the entire spectral range in terms of the wavenumber of the light is $3364.0486 \text{ cm}^{-1}$. In this numerical simulation, we intend to design the multi-grating with four sub-gratings to realize measurement of the spectral range. First, we must select four Littrow wavenumbers with uniform wavenumber spacing within the wavenumber range, with $\sigma_{1L} = 18400 \text{ cm}^{-1}$, $\sigma_{2L} = 17600 \text{ cm}^{-1}$, $\sigma_{3L} = 16800 \text{ cm}^{-1}$, and $\sigma_{4L} = 16000 \text{ cm}^{-1}$ being used here; by combining these wavenumbers with Eq. (2), the relationship for the groove density of the four sub-gratings can be written as:

$$1/d_1 : 1/d_2 : 1/d_3 : 1/d_4 = \sigma_{1L} : \sigma_{2L} : \sigma_{3L} : \sigma_{4L} = 23 : 22 : 21 : 20 \quad (35)$$

Based on the existing detector size parameters, the number of valid pixels $M \times N$ and the pixel size a on the detector are selected to be 2048×2048 and 0.0135 mm , respectively. On this basis, the maximum beam size that the detector can receive directly can be calculated to be $w_L = h_L = 27.6 \text{ mm}$. Other important parameters for the components used in this numerical simulation are listed in Table 1.

Table 1. Key Parameters of the Components Used in the Numerical Simulation

l_1	l_2	l_3	f_1	f_2	f_3	ε
160 mm	70 mm	50 mm	100 mm	10 mm	150 mm	0.01°
α_1	α_2	$1/d$	W_E	w_L	h_L	α_L
71.00°	17.00°	600 mm^{-1}	28.06 mm	27.60 mm	27.60 mm	10.4426°
M	N	m	n	a		
2048	2048	1/2	16	0.0135 mm		

By combining Eq. (35) with Eq. (1) and Eqs. (25)–(27) and using the parameters above, the groove densities of the four sub-gratings can be expanded in equal proportion by multiplying them with different magnifications to achieve different resolutions, effective wavenumber ranges (i.e., effective spectral ranges), and covering wavenumber ranges (i.e., covering spectral ranges), as shown in Table 2.

Analysis of the data given in Table 2 shows that greater magnification leads to a higher groove density and a higher corresponding resolution, but the effective wavenumber range and the covering wavenumber range are both narrower. When the groove density is enlarged to a certain extent, the resolution is high enough, but the effective wavenumber range is too narrow, which will then lead to the wavenumber range not being covered between the two adjacent sub-gratings, and thus will lead to discontinuity over the entire measurement range of the multi-grating. Using the grating design principle described in the previous section and the data presented in Tables 1 and 2, we can design a multi-grating with a wavenumber range from $15496.7319 \text{ cm}^{-1}$ to $18903.2681 \text{ cm}^{-1}$ and high spectral resolution of 0.4915 cm^{-1} when the magnification in Table 2 is 29, with an overall spectral range of $3406.5362 \text{ cm}^{-1}$. Each sub-grating has an effective

Table 2. Effective Wavenumber Ranges and Covering Wavenumber Ranges for Different Groove Densities

Magnification	$1/d_1$	$1/d_2$	$1/d_3$	$1/d_4$	δ_σ	Effective wavenumber range	Covering wavenumber range
1	23 mm ⁻¹	22 mm ⁻¹	21 mm ⁻¹	20 mm ⁻¹	14.4925 cm ⁻¹	29680.5879 cm ⁻¹	28880.5879 cm ⁻¹
8	184 mm ⁻¹	176 mm ⁻¹	168 mm ⁻¹	160 mm ⁻¹	1.8093 cm ⁻¹	3705.5043 cm ⁻¹	2905.5043 cm ⁻¹
15	345 mm ⁻¹	330 mm ⁻¹	315 mm ⁻¹	300 mm ⁻¹	0.9619 cm ⁻¹	1970.0291 cm ⁻¹	1170.0291 cm ⁻¹
22	506 mm ⁻¹	484 mm ⁻¹	462 mm ⁻¹	440 mm ⁻¹	0.6525 cm ⁻¹	1336.3291 cm ⁻¹	536.3291 cm ⁻¹
29	667 mm ⁻¹	638 mm ⁻¹	609 mm ⁻¹	580 mm ⁻¹	0.4915 cm ⁻¹	1006.5363 cm ⁻¹	206.5363 cm ⁻¹
36	828 mm ⁻¹	792 mm ⁻¹	756 mm ⁻¹	720 mm ⁻¹	0.3923 cm ⁻¹	803.3360 cm ⁻¹	3.3360 cm ⁻¹
43	989 mm ⁻¹	946 mm ⁻¹	903 mm ⁻¹	860 mm ⁻¹	0.3264 cm ⁻¹	664.8648 cm ⁻¹	none

wavenumber range of 1006.5363 cm⁻¹ and a covering wavenumber range of 206.5363 cm⁻¹ for every two adjacent sub-gratings.

To display the resolution of the MGCDSHS based on the designed multi-grating clearly, Table 3 presents the wavelength differences corresponding to the wavenumber differences in the different spectral regions. The data presented here indicate that the designed spectral resolution in terms of the wavelength is 0.0138 nm at around 530 nm, 0.0168 nm at around 585 nm, and 0.0205 nm at around 645 nm.

Table 3. Wavelength Difference versus Wavenumber Difference for Several Wavelengths

Wavelength	Wavenumber	Wavelength difference	Wavenumber difference
529.9736 nm	18868.8651 cm ⁻¹	529.9874 - 529.9736 = 0.0138 nm	18868.8651 - 18868.3736 = 0.4915 cm ⁻¹
529.9874 nm	18868.3736 cm ⁻¹	530.0012 - 529.9874 = 0.0138 nm	18868.3736 - 18867.8821 = 0.4915 cm ⁻¹
530.0012 nm	18867.8821 cm ⁻¹	530.0150 - 530.0012 = 0.0138 nm	18867.8821 - 18867.3906 = 0.4915 cm ⁻¹
530.0150 nm	18867.3906 cm ⁻¹		
584.9704 nm	17094.8836 cm ⁻¹	584.9872 - 584.9704 = 0.0168 nm	17094.8836 - 17094.3922 = 0.4915 cm ⁻¹
584.9872 nm	17094.3922 cm ⁻¹	585.0040 - 584.9872 = 0.0168 nm	17094.3922 - 17093.9007 = 0.4915 cm ⁻¹
585.0040 nm	17093.9007 cm ⁻¹	585.0208 - 585.0040 = 0.0168 nm	17093.9007 - 17093.4092 = 0.4915 cm ⁻¹
585.0208 nm	17093.4092 cm ⁻¹		
644.9700 nm	15504.5955 cm ⁻¹	644.9905 - 644.9700 = 0.0205 nm	15504.5955 - 15504.1040 = 0.4915 cm ⁻¹
644.9905 nm	15504.1040 cm ⁻¹	645.0110 - 644.9905 = 0.0205 nm	15504.1040 - 15503.6125 = 0.4915 cm ⁻¹
645.0110 nm	15503.6125 cm ⁻¹	645.0314 - 645.0110 = 0.0205 nm	15503.6125 - 15503.1210 = 0.4915 cm ⁻¹
645.0314 nm	15503.1210 cm ⁻¹		

Because the wavenumber ranges of the sub-gratings have been determined, it is vital to adjust the parameters of both the light beam and the reflection grating to ensure that the beam is distributed reasonably over the multi-gratings and to determine an appropriate size for the sub-gratings. As shown in Table 1, we selected cylindrical lens CL₁ with a focal length $f_1 = 100$ mm and cylindrical lens CL₂ with a focal length $f_2 = 10$ mm. According to Eq. (5), the beam size in the longitudinal plane can be reduced by 10 times. Using the tangent value of the angle of incidence in the longitudinal plane φ_{in} to represent the distribution of the incident light beams on the MGSHS, Fig. 7(a) shows the simulated curve for $\tan\varphi_{in}$ with different wavenumbers when diffracted by the reflection grating G_r with different values of the grating tilt angle α_1 and the incident light deflection angle α_2 when the grating line density $1/d_r$ is fixed and the beam positions corresponding to the maximum and minimum wavenumbers are distributed symmetrically. Analysis of the curves in Fig. 7(a) shows that the distribution curve of the light

beams changes rapidly at small wavenumbers but changes slowly at large wavenumbers; this phenomenon is particularly obvious when the deflection angle α_2 increases gradually from a negative value.

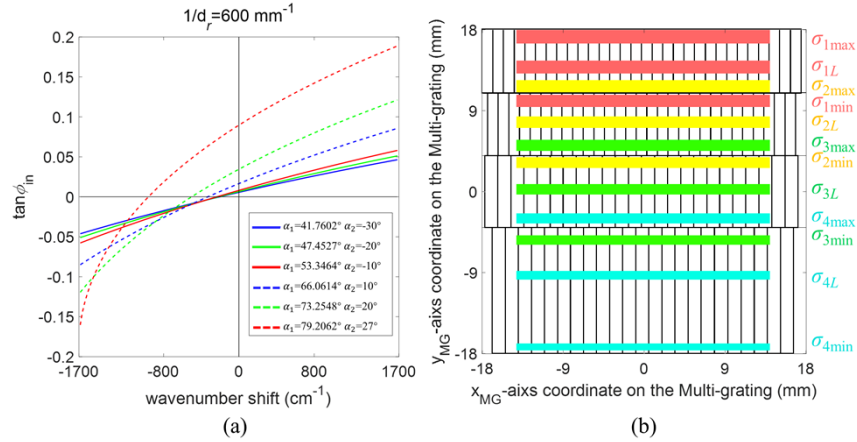


Fig. 7. (a) Relationships between $\tan\varphi_{in}$ and the wavenumber shift for different angles α_1 and α_2 when the groove density $1/d_r = 600 \text{ mm}^{-1}$, and (b) distributions of the light beams at the wavenumbers of $\sigma_{j\min}$, σ_{jL} , and $\sigma_{j\max}$ ($j = 1, 2, 3, 4$) when the parameters are determined.

On the basis of Eq. (8) and Eq. (15), the distributions of the centers of the light beams on the multi-gratings Y_{MG} and the detector planes Y_I , Y_{I1} , and Y_{I2} are related to $\tan\varphi_{in}$, and Y_{MG} in particular is proportional to $\tan\varphi_{in}$. Based on Eq. (34), the y_{mg} -axis position y_{Gj} and height h_{Gj} for each sub-grating on the multi-grating should adapt to the light beam distribution corresponding to its effective wavenumber range. If the $\tan\varphi_{in}$ curve changes too unevenly (as indicated by the green and red dotted lines in Fig. 7(a)), the height of the sub-grating with an effective wavenumber range at small wavenumbers will be too high, while the height of the sub-grating with an effective wavenumber range at large wavenumbers will be too small, and this is not conducive to fabrication of the multi-grating or to its adjustment in the optical path during the experiments. In addition, an uneven distribution curve will also lead to a compact interferogram distribution at large wavenumber and an unduly sparse interferogram distribution at small wavenumbers. Therefore, it is better to select appropriate values for α_1 and α_2 to obtain a $\tan\varphi_{in}$ curve that shows relatively smooth change for design of the multi-gratings and for the distribution of the interferograms that can be accepted by the detector.

As shown in Table 2, when α_1 , α_2 , and l_1 are determined, the main parameters of the sub-gratings and the multi-grating can be determined accordingly, and these parameters are shown in Table 4.

The distributions of the light beams at the wavenumbers $\sigma_{j\min}$, σ_{jL} , and $\sigma_{j\max}$ ($j = 1, 2, 3, 4$) on the multi-grating are shown in Fig. 7(b). The figure shows that the maximum and minimum wavenumbers corresponding to each effective wavenumber range are distributed reasonably on the sub-gratings; this not only ensures the continuity of the spectral range, meaning that all the wavenumbers can be detected, but also avoids losses in the throughput and the intensity. To provide a better illustration of the distribution and the production of the interferograms, the distributions of the light beams when diffracted by a single sub-grating and by two sub-gratings on the multi-grating are shown in Fig. 8.

By combining Eqs. (15)–(18) with the data in Tables 1 and 4, we are able to calculate the size parameters of the interferograms corresponding to the beam diffracted by one sub-grating, as shown in Table 5, and by two sub-gratings, as shown in Table 6. Table 5 shows that the minimum

Table 4. Key Parameters of the Sub-gratings on the Multi-grating

G_{i1}	σ_{1max}	σ_{1min}	σ_{1L}	$1/d_1$	h_{G1}	y_{G1}
	18903.2681 cm^{-1}	17896.7319 cm^{-1}	18400 cm^{-1}	667 mm^{-1}	7 mm	14.5 mm
G_{i2}	σ_{2max}	σ_{2min}	σ_{2L}	$1/d_2$	h_{G2}	y_{G2}
	18103.2681 cm^{-1}	17096.7319 cm^{-1}	17600 cm^{-1}	638 mm^{-1}	7 mm	7.5 mm
G_{i3}	σ_{3max}	σ_{3min}	σ_{3L}	$1/d_3$	h_{G3}	y_{G3}
	17303.2681 cm^{-1}	16296.7319 cm^{-1}	16800 cm^{-1}	609 mm^{-1}	8 mm	0 mm
G_{i4}	σ_{4max}	σ_{4min}	σ_{4L}	$1/d_4$	h_{G4}	y_{G4}
	16503.2681 cm^{-1}	15496.7319 cm^{-1}	16000 cm^{-1}	580 mm^{-1}	14 mm	-11 mm
MG_i	σ_{max}	σ_{min}	Δ_{MG}	w_{MG}	h_{MG}	y_{MG}
	18903.2681 cm^{-1}	15496.7319 cm^{-1}	3406.5362 cm^{-1}	36 mm	36 mm	0 mm

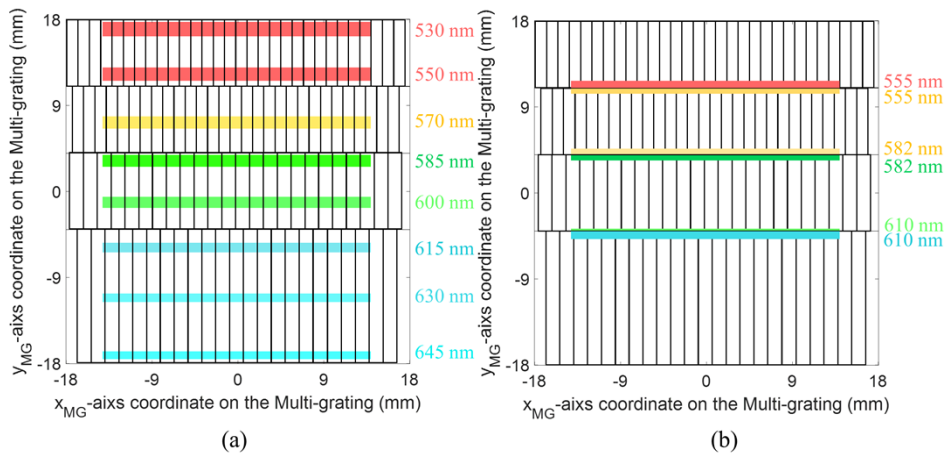


Fig. 8. Distributions of the light beams when (a) diffracted by one sub-grating at the wavelength in Table 5 and (b) diffracted by two sub-gratings at the wavelength in Table 6 on the multi-grating.

Table 5. Parameters of the Interferograms Corresponding to the Beam When Diffracted by One Sub-grating

Wavelength	Wavenumber	$y_l(\sigma)$	$h_l(\sigma)$	$w_l(\sigma)$
530 nm	18867.9 cm^{-1}	13.1119 mm	0.4708 mm	23.7598 mm
550 nm	18181.8 cm^{-1}	9.4754 mm	0.4401 mm	24.6153 mm
570 nm	17543.9 cm^{-1}	5.5927 mm	0.4074 mm	26.7574 mm
585 nm	17094.0 cm^{-1}	2.4741 mm	0.3808 mm	24.2172 mm
600 nm	16666.7 cm^{-1}	-0.8724 mm	0.3514 mm	26.0021 mm
615 nm	16260.2 cm^{-1}	-4.5151 mm	0.3197 mm	24.5473 mm
630 nm	15873.0 cm^{-1}	-8.5618 mm	0.2836 mm	25.5242 mm
645 nm	15503.9 cm^{-1}	-13.1988 mm	0.2420 mm	20.0451 mm

Table 6. Parameters of the Interferograms Corresponding to the Beam When Diffracted by Two Sub-gratings

Wavelength	Wavenumber	$y_{I1}(\sigma)$	$h_{I1}(\sigma)$	$w_{I1}(\sigma)$
555 nm	18018.2 cm ⁻¹	8.4869 mm	0.2593 mm	22.8892 mm
582 nm	17182.1 cm ⁻¹	3.0723 mm	0.2188 mm	22.6886 mm
610 nm	16393.4 cm ⁻¹	-3.3428 mm	0.0094 mm	22.5868 mm
Wavelength	Wavenumber	$y_{I2}(\sigma)$	$h_{I2}(\sigma)$	$w_{I2}(\sigma)$
555 nm	18018.2 cm ⁻¹	8.5983 mm	0.1618 mm	23.4490 mm
582 nm	17182.1 cm ⁻¹	3.1720 mm	0.1561 mm	23.2376 mm
610 nm	16393.4 cm ⁻¹	-3.2571 mm	0.3099 mm	22.8932 mm

height of the interferograms is $h_{I\min} = 0.2420$ mm, the minimum width of the interferograms is $w_{I\min} = 20.0451$ mm, and the interferograms that correspond to the maximum wavenumber and the minimum wavenumber are both located in the boundary of the detector plane, which meets the requirements of Eqs. (19)–(21) for the sizes and positions of the interferograms completely. Table 6 shows that the minimum summarized height of the mosaic interferograms $(h_{I1} + h_{I2})_{\min} = 0.3193$ mm, the minimum width of the first part of the mosaic interferograms $w_{I1\min} = 22.5868$ mm, and the minimum width of the second part of the mosaic interferograms $w_{I2\min} = 22.8932$ mm, which meets the requirements of Eqs. (31) and (32) for the sizes of the interferograms completely.

The interferograms generated by the MGCDSSHs that were recorded simultaneously on the detector plane corresponding to the results in Table 5 and Table 6 are shown in Fig. 9(a), and the detailed spectrum obtained from Fourier transform processing and analysis of the corresponding interferograms at the different positions on the detector plane in Fig. 9(a) is shown in Fig. 9(b). The interferogram can have an arbitrary wavelength dependent phase without affecting the recovery of the power spectral density. The red, yellow, green, and blue spectral lines in Fig. 9(b) represent the spectra as measured by sub-gratings G_{i1} , G_{i2} , G_{i3} , and G_{i4} , respectively. Figure 9(c) shows the measured spectrum of the entire spectral range produced by plotting all the individual spectra on the coordinate axis. Because of the coverage of the spectral range between each pair of adjacent sub-gratings and the existence of the mosaic interferograms, the individual spectra in Fig. 9(c) must be spliced, and the spectra in the covering spectral range must restore the peak intensity through superposition. The final spectrum generated by splicing and intensity reduction of all these spectra is shown in Fig. 9(d). Because these interferograms are separated, the problem of overlapping interferograms in traditional SHS is resolved, and this technique can prevent a high-intensity light beam at a specific wavelength from interfering with measurement of the interferogram of the other wavelengths; this is beneficial for detection of multiple spectral features and for weak spectral feature detection [26].

Based on the analysis above, we simulate the interferograms on the detector and corresponding detailed spectrum with a continuous incident spectrum in Fig. 10. From the simulation result on the detector in Fig. 10(a), we can clearly observe that the interferograms corresponding to the different spectral features are well separated, and the interferograms corresponding to the spectral features with relatively higher light intensity do not overlap the interferograms corresponding to the spectral features with lower light intensities around them. The blue curve in Fig. 10(b) is the detailed spectrum obtained from the Fourier transform of the interferograms in Fig. 10(a), which fits well with the normalized intensity of the incident spectrum, the weak spectral features next to the strong spectral features has also been well measured due to the separated interferograms.

In Table 4, the spectral resolutions at wavelengths around 530 nm, 585 nm, and 645 nm, which display the resolutions of the MGCDSSHs at the beginning, middle, and end of the measurement spectral range, are shown. To provide a better illustration of the spectral resolutions

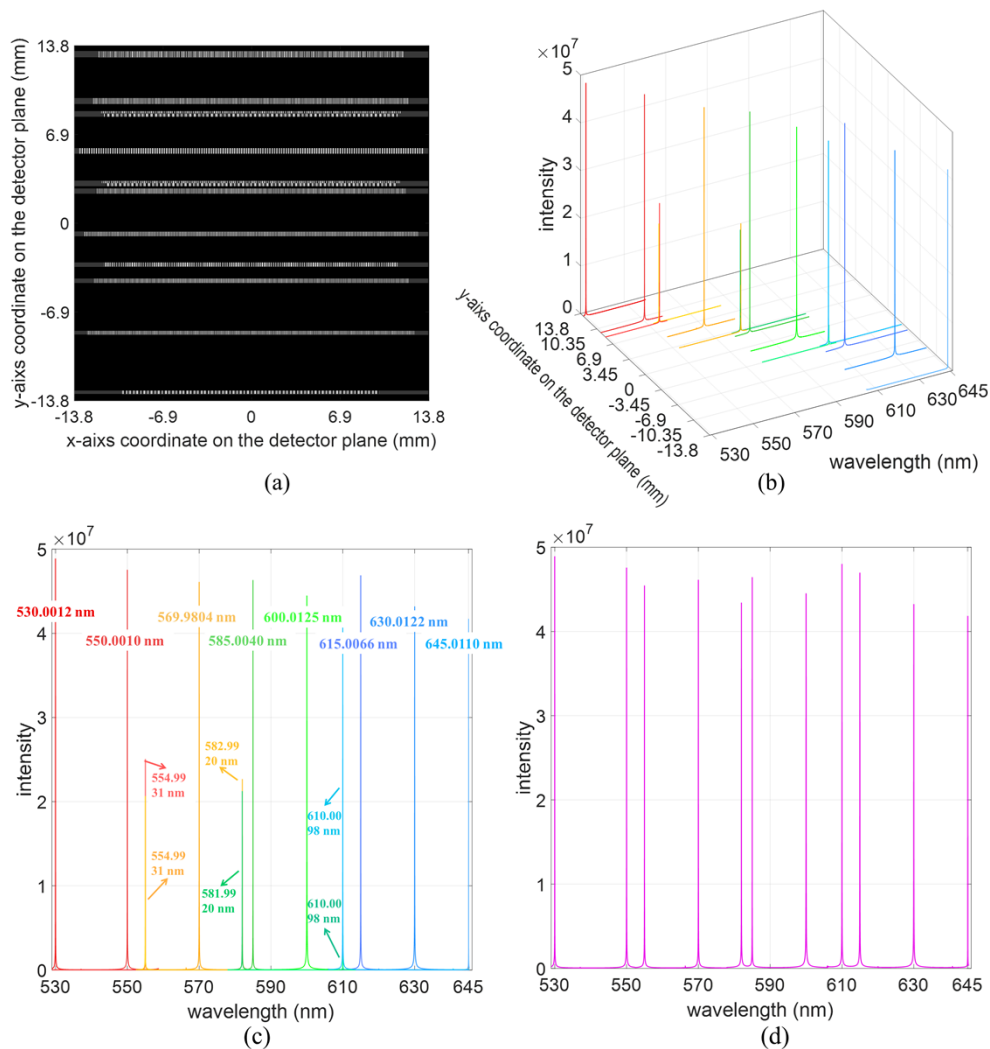


Fig. 9. (a) Several interferograms generated by the MGCDShS and recorded simultaneously on the detector. (b) Detailed spectrum obtained from Fourier transform processing of corresponding interferograms at different positions on the detector plane. (c) Direct spectrum for the entire measurement range of the MGCDShS. (d) Final spectrum generated by splicing and intensity reduction.

shown above, we simulated the interferograms and the detailed spectra corresponding to the wavelengths in Table 4, with results as shown in Fig. 11. Figure 11(a), 11(c), and 11(e) show the interferograms for the wavelengths around 530 nm, 585 nm, and 645 nm with equal intensities, respectively. The interferogram shown in Fig. 11(a) contains the wavelengths of 529.9736 nm, 529.9874 nm, 530.0012 nm, and 530.0150 nm only; the interferogram shown in Fig. 11(c) contains the wavelengths of 584.9704 nm, 584.9872 nm, 585.0040 nm, and 585.0208 nm only; and the interferogram shown in Fig. 11(e) contains the wavelengths of 644.9700 nm, 644.9905 nm, 645.0110 nm, and 645.0314 nm only.

The detailed spectra obtained from Fourier transform processing of the corresponding interferograms in Fig. 11(a), 11(c), and 11(e) are shown in Fig. 11(b), 11(d), and 11(f), respectively. In Fig. 11(b), the four peaks in the spectrum obtained correspond to the wavelengths

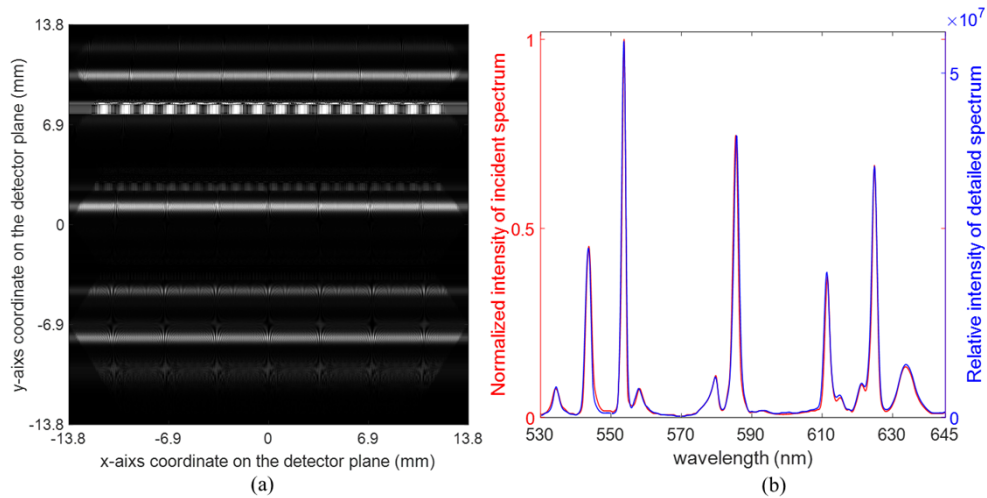


Fig. 10. (a) Several interferograms recorded simultaneously by the CDCDSHS with a continuous incident spectrum (b) Detailed spectrum obtained from the Fourier transform of these interferograms and the normalized intensity of incident spectrum.

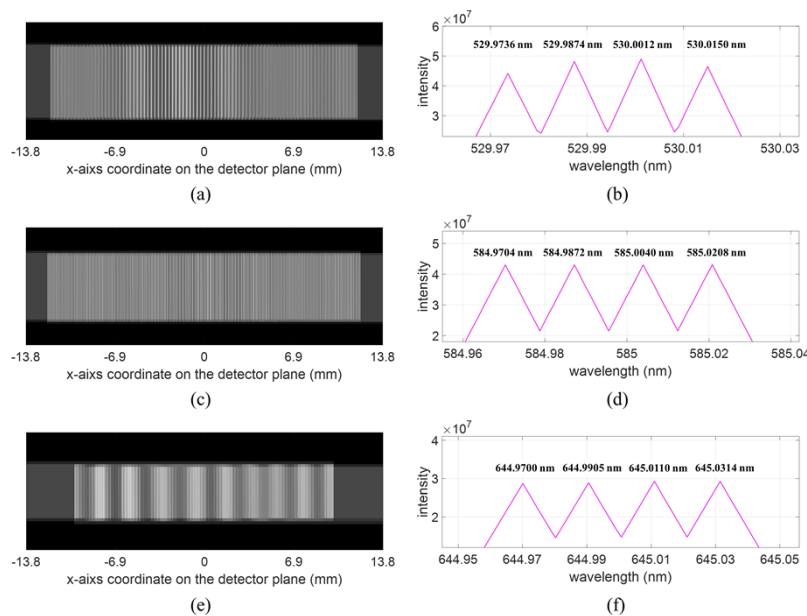


Fig. 11. Interferograms and detailed spectra obtained from Fourier transform processing of the interferograms for the wavelengths listed in Table 4 with equal intensity: (a) interferogram and (b) detailed spectrum containing the wavelengths of 529.9736 nm, 529.9874 nm, 530.0012 nm, and 530.0150 nm only; (c) interferogram and (d) detailed spectrum containing the wavelengths of 584.9704 nm, 584.9872 nm, 585.0040 nm, and 585.0208 nm only; and (e) interferogram and (f) detailed spectrum containing the wavelengths of 644.9700 nm, 644.9905 nm, 645.0110 nm, and 645.0314 nm of.

of 529.9736 nm, 529.9874 nm, 530.0012 nm, and 530.0150 nm, and the wavelength difference between each pair of adjacent peaks is 0.0138 nm. In Fig. 11(d), the four peaks in the spectrum obtained correspond to the wavelengths of 584.9704 nm, 584.9872 nm, 585.0040 nm, and

585.0208 nm, and the wavelength difference between each pair of adjacent peaks is 0.0168 nm. As shown in Fig. 11(f), the four peaks in the spectrum obtained correspond to the wavelengths of 644.9700 nm, 644.9905 nm, 645.0110 nm, and 645.0314 nm, and the wavelength difference between each pair of adjacent peaks is 0.0205 nm. From the analysis above, it can be concluded that the spectral resolution in terms of the wavelength of the designed MGCDSHS is 0.0138 nm around 530 nm, 0.0168 nm around 585 nm, and 0.0205 nm around 645 nm, and all spectral features within the spectral range can be detected.

4. Conclusion

In conclusion, we have demonstrated the modeling and calculation processes of the multi-grating-based cross-dispersion SHS (MGCDSHS) for two cases, where the light beam is diffracted by one sub-grating and where it is diffracted by two sub-gratings, and equations for the widths, heights, and locations of the interferograms in these two cases were derived. Then, based on the theoretical derivation above, an instrument design with a simulation of the MGCDSHS was presented.

In the numerical simulation, we designed a MGCDSHS based on a multi-grating that combines four sub-gratings to measure polychromatic incident light with a wavelength range from 530 nm to 645 nm. Based on the calculation results and analysis, a multi-grating design with a broad spectral range and high spectral resolution was obtained. The spectral resolution in wavelength terms is 0.0138 nm around 530 nm, 0.0168 nm around 585 nm, and 0.0205 nm around 645 nm. After the spectral performance design, we simulated the light beam distribution on the multi-grating and designed the size parameters of the different sub-gratings. Our analysis indicated that it is necessary to select appropriate parameters for the angle of incidence and the reflection grating to produce a reasonable distribution of the beams over the multi-grating and uniform separation of the interferograms on the detector.

According to the numerical simulation results, the designed MGCDSHS can record separated interferograms simultaneously that correspond to the different spectral features with high spectral resolution over a broad spectral range. Combining the lateral dispersion reflection grating with the longitudinal dispersion multi-grating not only resolves the mutual interference problem caused by overlapping of the interferograms that correspond to the different spectral features, but also provides both high spectral resolution and a broad spectral measurement range that cannot be achieved via single grating measurements. Replacing the conventional gratings with a multi-grating consisting of N_{MG} gratings with different groove densities breaks the mutual restriction between high spectral resolution and a broad spectral range that occurs in the conventional CDSHS. Additionally, with increasing N_{MG} , the spectral resolution and the spectral range of the MGCDSHS will become higher and broader, respectively, than those of the conventional CDSHS. The combination of the cylindrical lens group with the reflection grating can cause the light beams corresponding to the different spectral ranges to be diffracted by the corresponding sub-gratings on the multi-gratings without loss of throughput and also avoid intensity reduction of the fringes on the detector. In addition to these effects, the roll of one multi-grating around the central normal of its groove facet and the conical diffraction equation that was introduced for the first time in the SHS modeling process allows the interference fringe distribution to be calculated more accurately and makes the model suitable for multi-grating-based measurements by eliminating the ambiguity associated with the “true” and “ghost” spectra.

The MGCDSHS offers advantages that include high throughput, high spectral resolution, and a broad spectral range simultaneously while also requiring no moving parts. The MGCDSHS instrument has great potential for use in wide-range applications, including measurement of samples with multiple characteristic peaks, weak spectral measurements, and broadband and high-spectral-resolution measurements.

Funding. National Natural Science Foundation of China (52227810, 61975255, 62205333, U2006209); Jilin Province Research Projects in China (20220201083GX).

Disclosures. The authors declare no conflicts of interest.

Data availability. No data were generated or analyzed in the presented research.

Supplemental document. See [Supplement 1](#) for supporting content.

References

1. T. Dohi and T. Suzuki, "New type interference selective modulation spectroscopy," *Appl. Opt.* **10**(6), 1359–1362 (1971).
2. J. M. Harlander, *Spatial heterodyne spectroscopy: interferometric performance at any wavelength without scanning* (The University of Wisconsin-Madison, 1991).
3. P. Connes, "Spectromètre interférentiel à sélection par l'amplitude de modulation," *J. Phys. Radium* **19**(3), 215–222 (1958).
4. N. Lamsal and S. M. Angel, "Deep-Ultraviolet Raman Measurements Using a Spatial Heterodyne Raman Spectrometer (SHRS)," *Appl. Spectrosc.* **69**(5), 525–534 (2015).
5. N. Lamsal and S. M. Angel, "Performance Assessment of a Plate Beam Splitter for Deep-Ultraviolet Raman Measurements with a Spatial Heterodyne Raman Spectrometer," *Appl. Spectrosc.* **71**(6), 1263–1270 (2017).
6. G. Hu, W. Xiong, H. Shi, Z. Li, J. Shen, and X. Fang, "Raman spectroscopic detection for liquid and solid targets using a spatial heterodyne spectrometer," *J. Raman Spectrosc.* **47**(3), 289–298 (2016).
7. T. Schmid and P. Dariz, "Editorial for the Special Issue "Modern Raman Spectroscopy of Minerals,"" in *Minerals* (2020).
8. A. Zettner, A. B. Gojani, T. Schmid, and I. B. Gornushkin, "Evaluation of a Spatial Heterodyne Spectrometer for Raman Spectroscopy of Minerals," in *Minerals* (2020).
9. M. J. Egan, T. E. Acosta-Maeda, S. M. Angel, and S. K. Sharma, "One-mirror, one-grating spatial heterodyne spectrometer for remote-sensing Raman spectroscopy," *J. Raman Spectrosc.* **51**(9), 1794–1801 (2020).
10. O. R. Dawson and W. M. Harris, "Tunable, all-reflective spatial heterodyne spectrometer for broadband spectral line studies in the visible and near-ultraviolet," *Appl. Opt.* **48**(21), 4227–4238 (2009).
11. E. M. Kelly, M. J. Egan, A. Colón, S. M. Angel, and S. K. Sharma, "Remote Raman Sensing Using a Single-Grating Monolithic Spatial Heterodyne Raman Spectrometer: A Potential Tool for Planetary Exploration," *Appl. Spectrosc.*, 00037028221121304 (2022).
12. A. M. Colón, "The Development of a Monolithic Spatial Heterodyne Spectrometer for Extreme Environments," (2022).
13. W.-L. Zhang, Z.-Y. Liu, H. Wang, Y. Chen, Y. Wang, Z.-Z. Zhao, and T. Sun, "Research status of spatial Heterodyne spectroscopy—A review," *Microchem. J.* **166**, 106228 (2021).
14. P. B. Fellgett, "The nature and origin of multiplex Fourier spectrometry," *Notes Rec. R. Soc.* **60**(1), 91–93 (2006).
15. T. Hirschfeld, "Fellgett's Advantage in uv-VIS Multiplex Spectroscopy," *Appl. Spectrosc.* **30**(1), 68–69 (1976).
16. Y. Li, Y. Huang, Y. Wu, H. Li, X. Yang, Z. Li, and Z. Zhang, "Design of orthogonal tunable spatial heterodyne spectrometer based on prism dispersion," *Opt. Lasers Eng.* **162**, 107390 (2023).
17. G. Németh and Á. Pekker, "New design and calibration method for a tunable single-grating spatial heterodyne spectrometer," *Opt. Express* **28**(15), 22720–22731 (2020).
18. H. Sona and M. H. Walter, "Khayyam, a tunable, cyclical spatial heterodyne spectrometer on Mt. Hamilton," *J. Astronomical Telescopes Instruments, and Systems* **6**(1), 1–18 (2020).
19. J. Liu, X. Bayanheshig, S. Qi, C. Zhang, J. Sun, J. Zhu, X. Cui, and Li, "Backscattering Raman spectroscopy using multi-grating spatial heterodyne Raman spectrometer," *Appl. Opt.* **57**(33), 9735–9745 (2018).
20. J. Qiu, X. Qi, X. Li, Y. Tang, J. Lantu, X. Mi, and H. Bayan, "Broadband transmission Raman measurements using a field-widened spatial heterodyne Raman spectrometer with mosaic grating structure," *Opt. Express* **26**(20), 26106–26119 (2018).
21. J. Qiu, X. Li, and X. Qi, "Raman Spectroscopic Investigation of Sulfates Using Mosaic Grating Spatial Heterodyne Raman Spectrometer," *IEEE Photonics J.* **11**(5), 1–12 (2019).
22. J. Zhao and R. L. McCreery, "Multichannel FT-Raman Spectroscopy: Noise Analysis and Performance Assessment," *Appl. Spectrosc.* **51**(11), 1687–1697 (1997).
23. N. J. Overall and J. Howard, "Signal-to-Noise Considerations in FT-Raman Spectroscopy," *Appl. Spectrosc.* **43**(5), 778–781 (1989).
24. A. I. Sheinis, E. Mierkiewicz, F. Roesler, J. Harlander, and A. Bodkin, "A spatial heterodyne spectrometer for diffuse H-alpha spectroscopy," (SPIE, 2020), pp. 223–234.
25. M. J. Egan, A. M. Colón, S. M. Angel, and S. K. Sharma, "Suppressing the Multiplex Disadvantage in Photon-Noise Limited Interferometry Using Cross-Dispersed Spatial Heterodyne Spectrometry," *Appl. Spectrosc.* **75**(2), 208–215 (2021).
26. Q. Chu, X. Li, C. Jirigalantu, J. Sun, J. Chen, Y. Wang, Sun, and Bayanheshig, "Design study of a cross-dispersed spatial heterodyne spectrometer," *Opt. Express* **30**(7), 10547–10562 (2022).

27. Q. Pan, X. Chen, J. Zhou, Z. Zhao, and W. Shen, "Design and measurement of convex grating in conical diffraction Offner spectrometer," *Opt. Eng.* **58**(02), 1–025109 (2019).
28. J. E. Harvey and R. N. Pfisterer, "Understanding diffraction grating behavior: including conical diffraction and Rayleigh anomalies from transmission gratings," *Opt. Eng.* **58**(08), 1–087105 (2019).
29. Q. Yang, "Compact high-resolution Littrow conical diffraction spectrometer," *Appl. Opt.* **55**(18), 4801–4807 (2016).